Applied Thermal Engineering 225 (2023) 120183

Contents lists available at ScienceDirect

Applied Thermal Engineering

journal homepage: www.elsevier.com/locate/ate

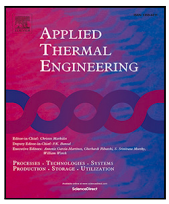

Research Paper

Reduced modeling of liquid desiccant falling film absorbers

Felix Hochwallner [a,b,*], Christoph Reichl [a,b], Johann Emhofer [a]

[a] AIT Austrian Institute of Technology GmbH, Center for Energy, Giefinggasse 2, 1210, Vienna, Austria
[b] TU Wien, Institute of Fluid Mechanics and Heat Transfer, Getreidemarkt 9, 1060, Vienna, Austria

ARTICLE INFO

Keywords:
Liquid desiccant
Dehumidification
Falling film
Absorber
Ionic liquids

ABSTRACT

Liquid desiccant falling film absorbers are an energy-efficient solution for humidity control and dehumidification in buildings and cold stores. This work presents a reduced one-dimensional physics-based modeling approach for this technology and compares it to a high-fidelity three-dimensional computational fluid dynamics (CFD) model. Both models capture the complex heat and mass transfer mechanisms of vertical falling films on two opposing walls and a horizontal crossflow of air. Additionally, both models were verified against experimental data from previous work, and the results showed good agreement within the uncertainties of the measurement equipment. A parameter variation study was also performed, comparing the results of both models under conditions relevant to cold store applications. The reduced model was found to be over 400 times faster than the high-fidelity model, while still achieving an average difference of less than ±0.14 K, ±1.3 %, and ±3.9 % for the calculated air outlet temperature, absorbed water vapor mass flow rate, and air-side pressure drop, respectively. The reduced model is suitable for optimization studies and easy to implement in system simulations, making it a valuable tool for the design and optimization of liquid desiccant systems.

1. Introduction

The use of air conditioning today accounts for nearly 20% of total electricity consumption in buildings around the world. This trend will intensify, due to rising living standards and as the world's economic and demographic growth becomes more concentrated in hotter countries [1]. Latent heat already covers a large portion of the total air conditioning load, especially in humid climates [2], and as building envelopes are improved with higher thermal resistance, humidity control may account for even a larger portion of the cooling load in the future as the sensible cooling load decreases while the latent load remains nearly constant [1]. Furthermore, dehumidification in cold storage warehouses shows great potential to prevent or delay condensation and frost formation, thus increasing the energy efficiency of the cooling system [3].

Dehumidification with absorbing liquid desiccant falling films is a promising alternative to current systems. Unlike conventional methods, these systems do not require the air flow to be cooled down to the dew point temperature, saving up to one-third of the energy for typical building application [4]. However, absorbing liquid desiccant falling film systems require additional components, e.g. pumps and fans, so they can still be less efficient than conventional systems if not properly designed. Numerical models can be used to predict the efficiency of desiccant systems for defined boundary conditions and thus optimize them. However, high computational costs should be avoided as they may prevent widespread use in system simulations.

Since the efficiency of the absorber significantly affects the overall efficiency of the dehumidification system, the modeling of falling film absorbers has received considerable attention in literature. Killion and Garimella [5] provide a review of modeling the coupled heat and mass transfer in falling film absorbers. Nakoryakov and Grigor'eva conducted remarkable research on film absorption for more than 20 years, and the assumptions they made are still used in much recent work [6]. They proposed an analytic solution for the combined heat and mass transfer problem during film absorption using a Fourier series, considering a uniform velocity in the solution film. Grossman [7] used essentially the same assumptions as Nakoryakov and Grigor'eva, but assumed a fully developed, laminar, Nusselt solution for the velocity profile of the solution film. He considered both an isothermal wall, as well as an adiabatic boundary condition at the back of the film. Park et al. [8] studied the heat and mass transfer between a falling desiccant film on a vertical plate and air in cross-flow and compared the numerical predictions with experimental results. They concluded that lower air flow rates provide better dehumidification and cooling, i.e. a lower humidity and temperature of the air at the outlet. Karami and Farhanieh [9] conducted a numerical study on the absorption of water vapor into a LiBr / water solution falling film along a vertical plate. They assumed

* Corresponding author at: AIT Austrian Institute of Technology GmbH, Center for Energy, Giefinggasse 2, 1210, Vienna, Austria.
E-mail address: felix.hochwallner@ait.ac.at (F. Hochwallner).

https://doi.org/10.1016/j.applthermaleng.2023.120183
Received 18 August 2022; Received in revised form 26 January 2023; Accepted 4 February 2023
Available online 11 February 2023

variable thermophysical properties of the solution and derived Nusselt and Sherwood numbers of the vertical plate absorber operating in the laminar regime. Hofmann and Kuhlmann [10] solved the coupled heat- and mass transfer of absorbing falling films using the flat-film approximation in a fully non-dimensional framework. They found an optimal Reynolds number in order to maximize the absorption efficiency, which can be interpreted as an optimal film thickness. Furthermore, they concluded that the waviness of the film has a greater impact on the mass transfer than variable thermophysical properties. Emhofer et al. [4] presented a mathematical model to predict the behavior of a cross-flow liquid-desiccant absorber using finite differences. Both a LiBr / water and an ionic liquid (IL) / water solution working pair are considered and the numerical predictions using the IL / water working pair are compared to experiments. They concluded that the length of the air channel, which corresponds to the width of the falling film, can be reduced to a certain value without much performance loss, while the optimal length depends on the operating conditions and the working pair, among other parameters. In 2019 Qi et al. [11] developed liquid–air mass transfer correlations for liquid desiccant dehumidification, considering the liquid/air contact and film instability. They verified their model by comparing it with experimental data of several widely-cited literature. To that end, they developed a correlation which is valid for a large variety of operating conditions. They concluded that the film instability and the wetting of the film significantly impacts the dehumidification performance. Furthermore, they concluded that reducing the contact angle of the falling film, therefore increasing the wettability, suppresses the film instability, but greatly increases the mass transfer.

More recently, Wen et al. [12] give a comprehensive review on the fundamentals and investigations of falling film dehumidification based on CFD (Computational Fluid Dynamics). Many studies exclusively address the description of the hydrodynamic behavior of falling film flow, while others also consider the coupled heat and mass transfer of falling film absorption. Since heat and mass transfer is the focus of this work, we will concentrate on those works. Luo et al. [13] developed a two-dimensional CFD model to predict the performance of counterflow adiabatic falling film absorbers using a LiCl / water solution. Penetration mass transfer theory was applied at the interface between the solution and the air and both the effects of wavy flow in the solution film as well as the variable physical properties of the solution and air were considered. Parametric studies were performed, and the simulation results showed that the solution flows in a continuous film on the plate once the velocity of the solution is large enough. Moreover, the simulated film thickness agrees well with the empirical Nusselt film formula. At higher absorbed water mass flow rates, the surface waves become more apparent on the solution film. In [14] Luo et al. extended their model for internally cooled dehumidifiers. They concluded that higher inlet temperatures of the desiccant reduce the dehumidification performance, not only by reducing the driving force for mass transfer, but also by shortening the contact time between the desiccant and the air as the viscosity of the desiccant decreases. It was shown, that internal cooling can significantly increase dehumidification performance and that accounting for variable physical properties of the solution results in slightly lower absorption. While the humidity of the air can be significantly reduced near the interface between the solution and the air, a high humidity content is maintained in the core of the air flow due to the limiting water vapor diffusion in the air. In [12] Wen et al. used a further extension of the model of [14] to propose approaches to improve dehumidification. They conclude that a super-hydrophilic coating can almost completely eliminate the shrinkage of the falling film and that curved fins can improve the momentum and mass transfer in the air flow by disturbing the flow, thus increasing the absorption performance. Reducing the duct width can further increase dehumidification performance, and a cross-flow configuration between air and solution is most favorable for dehumidification.

Unfortunately, none of the papers on CFD studies report the computational effort of the models. Since the works presented use CFD models with highly complex dynamics, a high computational effort is expected, which will most likely increase as the models are extended.

This contribution.

Main aim of this work is to build a computational cheap physics-based one-dimensional model of a liquid desiccant falling film absorber with vertical plates. The model shall be suitable to be used in system simulations included several additional components. To create such a model, first a high fidelity three-dimensional CFD model of a falling film is presented, which makes use of common assumptions as a non-wavy, stationary and laminar liquid film. Subsequently, a reduced one-dimensional model is derived from this high fidelity model. The reduced model uses empirical relationships for the heat and mass transfer, but considers its coupled nature. Following, both models are verified using measurement data from [4] for building application. Since the reduced model shall be used for system simulations at cold store conditions in future work, a parameter variation study was performed to compare both models at respective conditions.

Section 2 describes the methodologies of both numerical models and lists their limitations based on the assumptions made. In Section 3 the verification of both models using measurement data for building application and a comparison of both models for cold store application is shown. Finally, Section 4 concludes this work, by summarizing the most important results.

2. Methodology

To simulate the heat and mass transfer between moist air and a liquid desiccant/water solution film in an absorber or desorber, at least one solution film and half of the air channel have to be modeled. The entire component can then be described by upscaling the detailed solution.

2.1. CFD model

The CFD model is implemented into the open source CFD software package OpenFOAM [15] version 7 from the OpenFOAM Foundation. In the following sections the geometry, assumptions, governing equations, boundary and coupling conditions of the model are listed.

2.1.1. Geometry of the CFD model

The model consists of two regions, the air region and the region of the liquid solution. Fig. 1 shows the geometry of the CFD model. Due to the symmetry of the problem, only one vertical film and one half of the air channel are modeled, and a symmetry plane is defined at the half width of the air channel as a xz-plane at $y = L_y$. The air enters the domain at $x = 0$ and leaves it at $x = L_x$. In a crossflow to the air, the solution flows from $z = 0$ to $z = L_z$. The thickness of the solution results from the Nusselt profile and is thus denoted by δ_{Nu}, which is explained in Section 3.1.1. At $y = 0$, the interface between the air and the solution region is located. The air is considered as a binary mixture of the absorbate in a gaseous state (water vapor) and non absorbable gases (dry air) and the solution is a binary mixture of the absorbate in a liquid state (liquid water) and the liquid absorbent (desiccant). The absorbate, i.e. the water, undergoes a phase change at the interface, i.e. the film surface.

2.1.2. Assumptions of the CFD model

To simplify the problem appropriately, the following assumptions were made - almost analogous to [4]:

- Steady-state operation is considered.
- Both gases, the dry air and the water vapor, are assumed ideal.
- The thermophysical properties are constant throughout the simulation and are evaluated at the inlet conditions for both mixtures. This also includes the density and thus leads to incompressible flow in both regions. The heat of vaporization is evaluated at the solution inlet temperature and is also kept constant.
- A local thermodynamic equilibrium at the interface between the air and solution is considered.

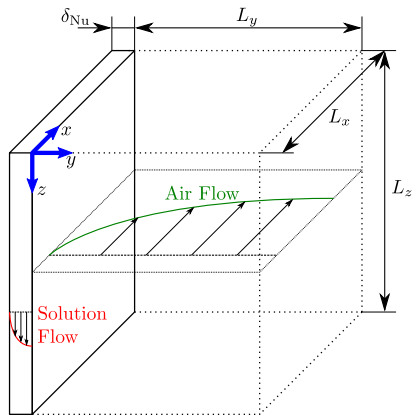

Fig. 1. Geometry of the falling film absorber CFD model. As the problem has a symmetry, only half of the air channel is modeled and the results are upscaled to describe the full channel.

- The interface between the air and solution is flat and indeformable.
- As the absorbed mass flow rate is significantly smaller than the solution mass flow rate, the thickness of the solution film is assumed to be constant.
- The absorbent is non-volatile.
- Independent hydrodynamic flows in the air and solution region are considered. For the air flow, the interface is assumed to be a wall at rest since the solution velocities are much smaller than the air velocities. For the solution flow, the gravitational forces exceed the induced shear forces of the air flow and the shear forces are therefore neglected.
- The air flow is predominantly driven by pressure, thus the gravitational forces on the air flow are neglected. Furthermore, as the air channel is significantly taller than wide ($L_z \gg L_y$), the air flow is considered to be independent of the absorber height, i.e., an undeveloped plane Poiseuille flow is assumed.
- Since the solution film thickness is much smaller than the absorber height ($L_z \gg \delta_{Nu}$), the solution flow is assumed to be fully developed in the entire domain.
- Viscous dissipation is neglected in both flows, as both flows are laminar.
- For the calculation of the specific humidity from the water vapor pressure in the air, a constant static air pressure of $p_a = p_{a,in}$ is assumed, since the fluctuations of the static air pressure are small.
- The enthalpy of mixing is small compared to the latent heat of phase change and is therefore neglected.

Contrary to the assumptions in [4], we do not neglect streamwise diffusion in either flow.

2.1.3. Governing equations of the CFD model

To describe the flow in the air region (subscript "a") a steady, laminar, single phase flow with constant density is assumed, where gravitational forces are neglected:

$$\vec{\nabla} \cdot \left(\rho_a \vec{u}_a\right) = 0, \tag{1a}$$

$$\vec{\nabla} \cdot \left(\vec{u}_a \vec{u}_a\right) - \vec{\nabla} \cdot \left(\nu_a \vec{\nabla} \vec{u}_a\right) = -\vec{\nabla} p_a, \tag{1b}$$

where ρ_a denotes the density, $\vec{u}_a$ the velocity vector, ν_a the kinematic viscosity and p_a the static pressure of the air.

With the assumptions of Section 2.1.2, the describing equations for the flow in the solution film (subscript "s") simplify to:

$$\partial_z u_{z,s} = 0, \tag{2a}$$

$$\nu_s \partial_y^2 u_{z,s} = -g, \tag{2b}$$

where $u_{z,s}$ denotes the solution velocity in z-direction, ν_s the kinematic viscosity of the solution and g the gravitational acceleration, fixed with $9.81\,\mathrm{m/s^2}$. The computation of the velocity field in both regions is independent of the heat and mass transfer and can therefore be solved in advance.

For both flows, convection–diffusion equations describe the transport of temperature and water content, where the subscript "i" represents a placeholder and indicates that the same equations apply for both regions.

$$\vec{\nabla} \cdot \left(\vec{u}\, T_i\right) = \kappa_i \vec{\nabla}^2 T_i, \tag{3a}$$

$$\vec{\nabla} \cdot \left(\vec{u}\, \chi_{w,i}\right) = D_i \vec{\nabla}^2 \chi_{w,i}, \tag{3b}$$

where T_i stands for the temperature, κ_i the thermal diffusivity, $\chi_{w,i}$ the water mass concentration and D_i the binary diffusion coefficient of water in the mixture. For the air flow, the water mass concentration represents the specific humidity and henceforth in this work, specific humidity will be used to denote the water mass concentration in the air flow.

2.1.4. Boundary conditions of the CFD model

The air enters the domain at the inlet ($x = 0$) with a uniform inlet velocity $u_{a,in}$ in x-direction and a constant temperature $T_{a,in}$ and relative humidity $\Phi_{a,in}$. At the outlet ($x = L_x$), the standard outflow conditions apply, i.e., the pressure is fixed at ambient pressure $p_{a,out} = p_{amb}$ and zero gradient conditions apply to the velocity field. The interface ($y = 0$) is assumed to be a wall at rest, so the non-slip condition holds and the symmetry condition is imposed at the center of the air gap ($y = L_y$).

At $z = 0$ the solution enters the domain with a mass flow rate $\dot{m}_{s,in}$ and a uniform inlet temperature $T_{s,in}$ and concentration $\chi_{d,s,in}$. In contrast to the air, the concentration of the solution is usually given by the mass concentration of the desiccant (subscript "d") and not of the water, where $\chi_{d,s} = 1 - \chi_{w,s}$. For better comparability with literature we adopt this notation. The solution is subject to the non-slip condition at the wall ($y = -\delta_{Nu}$) and the free-slip condition at the interface ($y = 0$).

2.1.5. Coupling conditions at interface in the CFD model

As stated in Section 2.1.2, we assume a local thermodynamic equilibrium at the interface, i.e. the film surface (subscript "fs"). Therefore, temperature and water vapor pressure at the film surface are equal for both fluids. The water vapor pressure of the solution is described by its vapor pressure field $p_{wv,s}$. Since the fluctuations of the solution pressure are small in open absorption systems, the vapor pressure field is considered independent of the solution pressure, depending only on the temperature and concentration of the solution. The vapor pressure at the film surface can thus be described by:

$$p_{wv,s,fs} = p_{wv,a,fs} = p_{wv,fs} = p_{wv,s,fs}\left(T_{s,fs}, \chi_{d,s,fs}\right). \tag{4}$$

Assuming both the water vapor as well as the dry air to be ideal gases, the specific humidity in the air flow at the film surface $\chi_{w,a,fs}$ can be obtained by the water vapor pressure at the film surface $p_{wv,fs}$ and the air pressure p_a:

$$\chi_{w,a,fs} = \frac{\gamma_a\, p_{wv,fs}}{p_a - (1 - \gamma_a)\, p_{wv,fs}}, \tag{5}$$

where γ_a is the ratio of the molar mass of water to the molar mass of dry air (subscript "da") $\gamma_a = \frac{M_w}{M_{da}} = 0.6225$. As the pressure fluctuations in the air flow are small, it is assumed that the static air pressure is constant $p_a = p_{a,in}$.

Kotchine's theorem [16] defines the jump conditions in specific enthalpy $h \propto c_p T$ and concentration χ at the film surface:

$$\left[\lambda\, \partial_n T\right] = \dot{\varphi}\,[h], \tag{6a}$$

$$\left[\rho\, D\, \partial_n \chi\right] = \dot{\varphi}\,[\chi], \tag{6b}$$

where c_p is the specific isobaric heat capacity, λ the thermal conductivity and $\dot{\varphi}$ the mass flux across the film surface. ∂_n denotes the surface

normal derivative, where the normal vector $\vec{n}$ is pointing into the air region. For any quantity Z, the jump brackets are defined as $[Z] = Z_s - Z_a$. The jump in enthalpy $[h]$ stems from the fact that latent heat is transferred at the interface due to the phase change of the absorbate, i.e. the water. While mass conservation dictates $[\dot{\varphi}] = 0$, the jump in concentration is related to the different definition of concentration in the two binary mixtures, i.e., the moist air and the solution film.

The heat flow rate coupling condition at the film surface results from the jump condition of the specific enthalpy (6a):

$$\lambda_s \, \partial_n T_s - \lambda_a \, \partial_n T_a = \dot{\varphi} \underbrace{\left(h_s - h_a\right)}_{-\Delta h_v}, \tag{7}$$

where Δh_v is the heat of vaporization. The jump condition for the concentration (6b) generally applies to all mixture components. However, it is advantageous to write it for the mixture components that are present in only one region, i.e. the desiccant and the dry air, to reduce the amount of terms in the equations:

$$\rho_s \, D_s \, \partial_n \chi_{d,s} = \dot{\varphi} \, \chi_{d,s}, \tag{8a}$$

$$\rho_a \, D_a \, \partial_n \chi_{da,a} = \dot{\varphi} \, \chi_{da,a}. \tag{8b}$$

Considering the relations for the concentrations and their gradients in the mixtures, i.e. $\chi_{d,s} + \chi_{w,s} = 1$ and $\partial_n \chi_{d,s} + \partial_n \chi_{w,s} = 0$ in the solution region and $\chi_{da,a} + \chi_{w,a} = 1$ and $\partial_n \chi_{da,a} + \partial_n \chi_{w,a} = 0$ in the air region, relations for the mass flux that depend on the water concentrations are obtained:

$$\dot{\varphi} = -\frac{\rho_s \, D_s \, \partial_n \chi_{w,s}}{1 - \chi_{w,s}} = -\frac{\rho_a \, D_a \, \partial_n \chi_{w,a}}{1 - \chi_{w,a}}. \tag{9}$$

Due to the choice of the direction of the normal vector, a positive mass flux $\dot{\varphi} > 0$ means a mass flux from the solution to the air, i.e. a desorption.

2.1.6. Limitations of the CFD model

Based on the assumptions made, the following limitations of the CFD model should be considered:

- As steady-state operation, a constant film thickness and a flat and indeformable interface is assumed, film instability is not considered. Film instability becomes especially important for high Reynolds number solution flows, as stated in [11].
- A fully wetted wall is assumed. This is important if comparing the results to experiments.
- The model does not consider the effect of the air flow on the solution flow and vice versa. Therefore, velocity changes due to shear forces are not considered.
- Both the air and solution flow are considered laminar. This is a reasonable limitation, since higher air velocities, which would lead to turbulent air flow, would cause undesirably high pressure losses and possible carryover of the solution film. Both must be avoided in the applications considered here.
- We assumed constant thermophysical properties. However, especially the viscosity of the solution shows large variations with respect to the temperature and concentration. Bo et al. [17] showed that for a single simulation of a counter-flow absorber, the prediction of the total absorption mass flow rate is about 6.5% higher when assuming constant thermophysical properties.

Data from the literature [10,11,14,17] suggests that film instability has a greater influence on the absorption mass flow rate, than variable thermophysical properties. Thus, an extension of the model would have to consider this as a priority.

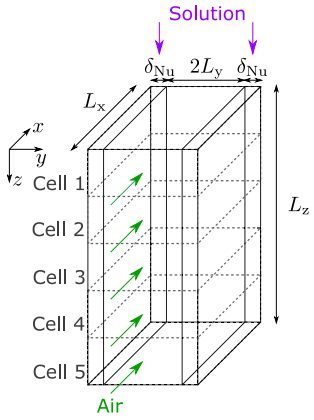

Fig. 2. Geometry of the reduced falling film absorber model. Contrary to the geometry of the CFD model (Fig. 1), the full air gap and two opposing solution films are modeled.

2.2. Reduced model

The reduced one-dimensional model was written in the modeling language Modelica 4.0.0 [18] and the simulation environment Dymola version 2020 from Dassault Systèmes [19] was used. Furthermore, the TIL Suite of TLK-Thermo GmbH [20] was utilized, which is specialized in the simulation of thermal systems. In the next sections the geometry, assumptions and governing equations of the reduced model are listed.

2.2.1. Geometry of the reduced model

Contrary to the CFD model, the reduced model does not consider a symmetry at the center of the air gap, so the full air gap and two opposing solution films are modeled. The domain is discretized in z-direction only and each cell contains an air and a solution region. Fig. 2 shows the geometry of the reduced model. For the visualization a discretization in five cells was assumed, however, a different number of cells may be used for the computation.

The total air flow is divided into equally sized parallel air flows, with all cells having the same input state. At the output of the cells, all these parallel air flows are summed up again into a single air flow satisfying the mass, momentum and energy balance.

The solution flow enters the first cell and is forwarded to the next cells until it reaches the outlet at $z = L_z$. The air and the solution regions are coupled at the interface, i.e. at the film surface, by both heat and mass transfer.

2.2.2. Assumptions of the reduced model

In addition to the assumptions of the CFD model, the following assumptions are made for the reduced model:

- Heat transfer from the air to solution flow is described by correlations from literature for a plane Poiseuille flow with fixed wall temperatures and undeveloped thermal and hydraulic flow profiles at the inlet.
- Mass transfer from the air to solution flow is described by the Lewis analogy, therefore the mass transfer coefficient is derived from the heat transfer coefficient.
- Heat transfer in the solution film is described exclusively by heat conduction, as the solution film is very thin compared to its other geometric dimensions ($\delta_{Nu} \ll L_x$ and $\delta_{Nu} \ll L_z$) and the fluid velocities are small. This only applies to the description of the heat transfer, the energy balance is not violated.

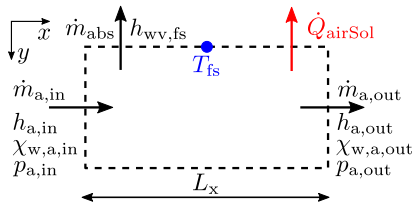

Fig. 3. Inputs and outputs of the control volume in the air region for one discretization cell in z-direction.

2.2.3. Governing equations of the reduced model

Each cell of the reduced model contains both an air and a solution region. While the domain is discretized in z-direction (direction of the solution flow), equations describing the distribution of temperature and mass concentration in the x-direction (direction of the air flow) and y-direction (direction perpendicular to both flows) need to be found. In the following paragraphs, the governing equations for the control volumes of the air and solution region in a single discretization cell are listed.

Air region.

Fig. 3 shows the inputs and outputs of the air region, where the subscript "in" indicates the inlet and "out" the outlet. The absorbed water vapor mass flow rate from the air to the solution is denoted with $\dot{m}_{abs}$, the transferred heat flow rate with $\dot{Q}_{airSol}$ and the film surface temperature with T_{fs}.

Two mass balances need to be fulfilled for the air flow. We have chosen one for the moist air mass, and one for the absorbate, i.e. the water vapor:

$$\dot{m}_{a,in} = \dot{m}_{a,out} + \dot{m}_{abs}, \tag{10a}$$

$$\underbrace{\chi_{w,a,in}\,\dot{m}_{a,in}}_{\dot{m}_{wv,in}} = \underbrace{\chi_{w,a,out}\,\dot{m}_{a,out}}_{\dot{m}_{wv,out}} + \dot{m}_{abs}, \tag{10b}$$

where $\dot{m}_a$ denotes the moist air mass flow rate.

In air conditioning application it is beneficial to relate properties to the dry air mass, as it does not change in most components, contrary to the moist air mass. To guarantee conservation of mass, the dry air mass flow rate must be the same at both the inlet and the outlet:

$$\dot{m}_{da} = \dot{m}_{a,in}\left(1-\chi_{w,a,in}\right) = \dot{m}_{a,out}\left(1-\chi_{w,a,out}\right), \tag{11}$$

where $\dot{m}_{da}$ denotes the dry air mass flow rate.

The water mass fraction related to the dry air mass is called the humidity ratio. It can be derived from the water mass fraction related to the moist air mass, i.e. the specific humidity, by:

$$X_a = \frac{\chi_{w,a}}{1-\chi_{w,a}}, \tag{12}$$

where X_a denotes the humidity ratio, defined as water vapor mass per dry air mass.

The energy balance of the air region includes the enthalpy flow rate at the inlet $\dot{m}_{a,in}\,h_{a,in}$, outlet $\dot{m}_{a,out}\,h_{a,out}$ and film surface $\dot{m}_{abs}\,h_{wv,fs}$ and additionally the transferred sensible heat flow rate at the film surface $\dot{Q}_{airSol}$:

$$\dot{m}_{a,in}\,h_{a,in} - \dot{m}_{a,out}\,h_{a,out} = \dot{Q}_{airSol} + \dot{m}_{abs}\,h_{wv,fs}. \tag{13}$$

To find an equation for the absorbed mass flow rate $\dot{m}_{abs}$ one can rewrite the mass balance of the water vapor (10b) for an infinite small length dx, using Eqs. (11) and (12):

$$\underbrace{\dot{m}_{da}\left(X_a(x)-X_a(x+dx)\right) - 2\,\beta_{airSol}\,\rho_a\,L_z\left(X_a(x)-X_{a,fs}\right)dx}_{\dot{m}_{abs}\,|_x^{x+dx}} = 0, \tag{14}$$

where β_{airSol} denotes the mass transfer coefficient between the air and solution flow and $X_{a,fs}$ the humidity ratio of the air at the film surface. The term $\dot{m}_{abs}\,|_x^{x+dx}$ represents the absorbed mass flow rate from x to $x+dx$ and the factor 2 comes from the fact that there are two opposing falling films. Substituting $X_a(x+dx)$ by its Taylor series, considering only the first order term and dividing by $\dot{m}_{da}\,dx$, one obtains a first order differential equation:

$$\frac{\partial X_a}{\partial x} - \frac{2\,\beta_{airSol}\,\rho_a\,L_z}{\dot{m}_{da}}X_a + \frac{2\,\beta_{airSol}\,\rho_a\,L_z}{\dot{m}_{da}}X_{a,fs} = 0, \tag{15}$$

with the boundary conditions:

$$X_a(x=0) = X_{a,in},\; X_a(x\to\infty) = X_{a,fs}. \tag{16}$$

By neglecting the higher order terms in the Taylor series, Eq. (15) can be solved analytically:

$$X_a(x) = X_{a,fs} + \left(X_{a,in}-X_{a,fs}\right)\exp\left(-\frac{2\,\beta_{airSol}\,\rho_a\,L_z}{\dot{m}_{da}}x\right). \tag{17}$$

The total absorbed mass flow rate $\dot{m}_{abs} = \dot{m}_{abs}\,|_0^{L_x}$ can then be described by:

$$\dot{m}_{abs} = \dot{m}_{da}\left(1-\exp\left(-\frac{\beta_{airSol}\,\rho_a\,A_{airSol}}{\dot{m}_{da}}\right)\right)\left(X_{a,in}-X_{a,fs}\right), \tag{18}$$

with $A_{airSol} = 2\,L_z\,L_x$ the total area between the air and solution flow.

A similar approach can be taken in order to give an equation for the transferred sensible heat $\dot{Q}_{airSol}$. By rewriting Eq. (13), splitting the moist air enthalpy flow into dry air and water vapor and assuming constant specific isobaric heat capacities, one obtains:

$$\begin{aligned}&\dot{m}_{da}\left(c_{p,da} + X_{a,in}\,c_{p,wv}\right)\Delta T_{a,in} -\\ &\dot{m}_{da}\left(c_{p,da} + X_{a,out}\,c_{p,wv}\right)\Delta T_{a,out} -\\ &\qquad \dot{m}_{abs}\,c_{p,wv}\,\Delta T_{fs} = \dot{Q}_{airSol},\end{aligned} \tag{19}$$

where $c_{p,da}$ denotes the specific isobaric heat capacity of dry air and $c_{p,wv}$ the specific isobaric heat capacity of the water vapor. The Δ in front of the temperatures state that the temperatures are related to a common reference temperature $\Delta T_i = T_i - T_{ref}$. Using Eqs. (10)–(12), Eq. (19) can be rewritten to:

$$\begin{aligned}&\overbrace{\dot{m}_{da}\left(c_{p,da} + X_{a,in}\,c_{p,wv}\right)}^{\dot{m}_{a,in}c_{p,a,in}}\left(T_{a,in}-T_{a,out}\right) +\\ &\qquad \dot{m}_{abs}\,c_{p,wv}\left(T_{a,out}-T_{fs}\right) = \dot{Q}_{airSol},\end{aligned} \tag{20}$$

where $c_{p,a,in}$ stands for the specific isobaric heat capacity of moist air at the inlet conditions. The second term in this equation accounts for the fact that the absorbed water vapor is being cooled or heated to T_{fs} and not to $T_{a,out}$, contrary to the remaining moist air. For regular absorption and desorption, the heat capacity rate of the moist air $\dot{m}_{da}\left(c_{p,da} + X_A c_{p,wv}\right)$ is significantly greater than the heat capacity rate of the absorbed water vapor $\dot{m}_{abs}c_{p,wv}$, while the temperature differences $T_{a,in}-T_{a,out}$ and $T_{a,out}-T_{fs}$ are of the same order. By neglecting the absorbed water vapor term, the heat flow equation is separated from the mass flow equation, thus it is possible to solve both equations analytically. In Appendix A we show that for typical operating conditions, the magnitude of the absorbed water vapor term is mostly well below 1% of the magnitude of the moist air term. After neglecting the absorbed water vapor term, the energy balance for an infinitesimally small length dx reads:

$$\begin{aligned}&\dot{m}_{a,in}\,c_{p,a,in}\left(T_a(x)-T_a(x+dx)\right) +\\ &2\,\alpha_{airSol}\,L_z\left(T_{fs}-T_a(x)\right)dx = 0,\end{aligned} \tag{21}$$

where α_{airSol} is the heat transfer coefficient between the air flow and the film surface. Substituting $T_a(x+dx)$ by its Taylor series, considering only the first-order term, and dividing it by $\dot{m}_{a,in}c_{p,a,in}dx$, one obtains a first-order differential equation:

$$\frac{\partial T_a}{\partial x} - \frac{2\,\alpha_{airSol}\,L_z}{\dot{m}_{a,in}\,c_{p,a,in}}T_a + \frac{2\,\alpha_{airSol}\,L_z}{\dot{m}_{a,in}\,c_{p,a,in}}T_{fs} = 0, \tag{22}$$

with the boundary conditions:

$$T_a(x=0) = T_{a,in}, T_a(x \to \infty) = T_{fs}. \tag{23}$$

Again, Eq. (22) can be solved analytically as the higher order terms are neglected:

$$T_a(x) = T_{fs} + \left(T_{a,in} - T_{fs}\right) e^{-\frac{2\,\alpha_{airSol}\,L_z}{\dot{m}_{a,in}\,c_{p,a,in}}x}, \tag{24}$$

and therefore, the sensible heat transferred from the air to the solution can be described by:

$$\dot{Q}_{airSol} = \dot{m}_{a,in}\,c_{p,a,in}\left(1 - e^{-\frac{\alpha_{airSol}\,A_{airSol}}{\dot{m}_{a,in}\,c_{p,a,in}}}\right)\left(T_{a,in} - T_{fs}\right). \tag{25}$$

The heat transfer from the air to the solution flow is described by Nusselt correlations from literature, considering a planar gap flow. For fixed wall temperatures and a non-developed thermal and hydraulic flow profile at the inlet, Stephan [21] gives the following relation:

$$Nu_{airSol} = 7.55 + \frac{0.024\left(Re\,Pr_a\,d_h/L_x\right)^{1.14}}{1 + 0.0358\left(Re\,Pr_a\,d_h/L_x\right)^{0.64}\,Pr_a^{0.17}}, \tag{26}$$

where Nu_{airSol} is the Nusselt number for the whole length for the heat transfer from the air to the solution flow, Re is the Reynolds number related to the hydraulic diameter d_h and Pr_a is the Prandtl number of the air. The Nusselt number and Reynolds number are defined as:

$$Nu_{airSol} = \frac{\alpha_{airSol}\,d_h}{\lambda_a},\ Re = \frac{u_{a,in}\,d_h}{\nu_a}. \tag{27,28}$$

The mass transfer coefficient is obtained from the heat transfer coefficient using the Lewis analogy, as described by Baehr H. D. and Stephan K. [22]:

$$\beta_{airSol} = \frac{\alpha_{airSol}}{\rho_a\,c_{p,a}}Le_a^{-2/3}, \tag{29}$$

where Le_a denotes the Lewis number of the air. It should be stated that the mass transfer coefficient obtained by the Lewis analogy is related to the difference in mass fraction, rather than the humidity ratio, as it is used in Eq. (14). However, in this work the mass transfer coefficient, as obtained by the Lewis analogy, is used as if it was related to the difference in the humidity ratio. In Appendix B we show that the difference between the specific humidity and the humidity ratio is very small, especially for application with low air temperatures. However, this simplification allows the heat and mass flow rates to be solved analytically.

The momentum balance in the air flow can simply be written in terms of the pressures at the inlet and outlet:

$$p_{a,in} - p_{a,out} = \Delta p_a, \tag{30}$$

where p_a denotes the static pressure and Δp_a the pressure drop. The pressure drop is evaluated using a pressure drop model for a plane Poiseuille flow with an undeveloped flow profile at the inlet. Stephan K. [21] gives an asymptote for the pressure drop for large gap lengths L_x:

$$\Delta p_a = \underbrace{\frac{3\,\eta_a\,u_{a,in}\,L_x}{L_y^2}}_{\Delta p_{a,friction}} + \underbrace{\frac{8}{25}\rho_a\,u_{a,in}^2}_{\Delta p_{a,developing}}, \tag{31}$$

where η_a is the dynamic viscosity of air with $\eta_a = \nu_a\,\rho_a$. The first term $\Delta p_{a,friction}$ describes the pressure drop for a fully developed Poiseuille flow due to friction, while the second term $\Delta p_{a,developing}$ denotes the additional pressure drop due to a non developed flow profile at the inlet.

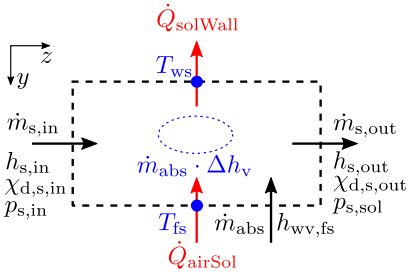

Fig. 4. Inputs and outputs of the control volume in the solution region for one discretization cell in z-direction.

Solution region.

Fig. 4 shows the inputs and outputs of the solution region. The interface to the wall is called the wall surface (subscript "ws").

As in the air region, two mass balances must be fulfilled. We chose one for the total solution flow and one for the desiccant flow. This gives the two mass balances:

$$\dot{m}_{s,in} + \dot{m}_{abs} = \dot{m}_{s,out}, \tag{32}$$

$$\underbrace{\chi_{d,s,in}\,\dot{m}_{s,in}}_{\dot{m}_{d,in}} = \underbrace{\chi_{d,s,out}\,\dot{m}_{s,out}}_{\dot{m}_{d,out}}, \tag{33}$$

where $\dot{m}_s$ denotes the total solution mass flow rate.

The energy balance of the solution region contains the sensible heat transferred at the film surface $\dot{Q}_{airSol}$ and at the wall $\dot{Q}_{solWall}$, and the enthalpy flow at the film surface $h_{wv,fs}$ and at the inlet $h_{s,in}$ and outlet $h_{s,out}$:

$$\dot{Q}_{airSol} + \dot{m}_{abs}\,h_{wv,fs} + \dot{m}_{s,in}\,h_{s,in} = \dot{Q}_{solWall} + \dot{m}_{s,out}\,h_{s,out}. \tag{34}$$

The specific enthalpy of the solution consists of a desiccant part h_d, a water part h_w and the latent heat of phase change Δh_v:

$$h_s = \chi_{d,s}\,h_d + \left(1 - \chi_{d,s}\right)\left(h_w - \Delta h_v\right), \tag{35}$$

where the enthalpy of mixing is neglected, as it is small compared to the latent heat of phase change.

The heat transfer in the solution film is approximated by heat conduction only:

$$\overbrace{\dot{m}_{abs}\Delta h_v}^{\dot{Q}_{latent}} + \dot{Q}_{airSol} = \frac{\lambda_s}{\delta_{Nu}/2}A_{airSol}\left(T_{fs} - T_s\right), \tag{36a}$$

$$\dot{Q}_{solWall} = \frac{\lambda_s}{\delta_{Nu}/2}A_{solWall}\left(T_s - T_{ws}\right), \tag{36b}$$

where $\dot{Q}_{latent}$ denotes the transferred latent heat flow rate, λ_s the thermal conductivity of the solution film, $A_{solWall}$ the area between the solution and the wall, T_{ws} the wall surface temperature and T_s an arbitrary solution temperature, which was chosen to be the outlet solution temperature $T_s = T_{s,out}$.

2.2.4. Limitations of the reduced model

Since the model was derived from the CFD model based upon the same assumptions, it is also subject to the same constraints listed in Section 2.1.6. Additionally to the limitations of the CFD model, the following limitations apply to the reduced model:

- A Nusselt correlation for a planar gap flow with fixed wall temperatures (26) is used for the heat transfer from the air to the solution flow. However, the solution film has a non-uniform temperature distribution along the x-axis. This error gets more pronounced with increasing sensible and latent heat transfer.

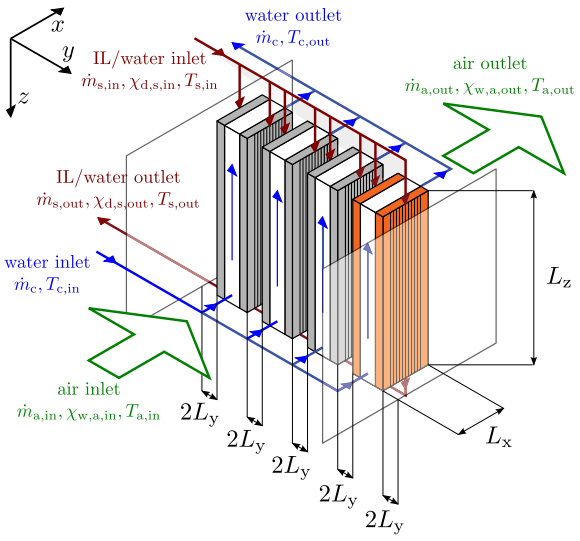

Fig. 5. Schematics of the experimental setup. The ionic liquid (IL)/water solution flows from top to bottom, with the cooling water in counterflow and the air in crossflow. This figure is taken from [4] but with a modified coordinate system.

- The heat transfer in the solution flow is described exclusively by heat conduction, where the heat conduction equation is separated into two parts, as stated in Eqs. (36). The first part describes the heat transfer from the wall to the middle of the solution film and the second part describes the heat transfer from the middle to the interface with the air flow. By that, both a fixed wall temperature and an adiabatic wall can be modeled. However, the linear approximation of the temperature distribution in the solution film leads to larger errors for thicker solution films and higher latent heat transfer.

2.3. Experiments

In a previous work by one of the authors, experiments were conducted on the use of liquid desiccant falling film absorbers in building applications. In the present work, these experiments were used to verify the numerical models created. In the following sections, the experimental setup and the differences between the experiments and the models are listed. For more information on the experiments, see the work by Emhofer et al. [4].

2.3.1. Experimental setup

Fig. 5 shows the schematic of the experimental setup. The plates (shown in gray and brown) have a thickness of 3 mm, and the gap between the plates and between the outer plates and the casing is $2\,L_y = 4$ mm. Height of the channel and plates is $L_z = 0.7$ m and the channel length is $L_x = 0.1$ m. The mass flow rate of the solution was increased until the plates were completely wetted by the solution and was set slightly above this minimum mass flow rate to $1.768 \cdot 10^{-3}$ kg/s.

As desiccant an available ionic liquid (IL) from *Evonik Industries AG* was chosen, as it is non-corrosive, non-hazardous, and does not pose any crystallization problems. A stack of eight parallel plates was assembled to hold the liquid film, while two plates share a common water-cooling channel.

2.3.2. Differences of the experiments to the numerical models

Differences between the experiments and the numerical models, which may lead to deviations in the results, are listed here:

- In the experiments, the backplates had vertical grooves to direct the solution flow and prevent dewetting due to the shear forces of the air flow. The grooves had a semicircular cross-section with a radius of 0.25 mm. In the numerical models, the back plates are assumed to be flat. As shown in [4], diffusion of water in the solution film does not significantly limit absorption, so the film thickness does not critically affect the absorption process.
- Since most of the solution flows within the grooves, as shown in [23], the vertical plates were separated by $2L_y$ in the experiments, disregarding the thickness of the solution film.
- For the numerical models, each air channel has two opposing solution films. However, for the outermost air channels in the experiments, there is no opposing film. As shown in [4], the absorption is limited by the diffusion of water vapor perpendicular to the air flow, which means that the air near the film surface becomes very dry, but a humid core flow still remains. As long as the water concentration in the center of the air channel does not change significantly, the asymmetry of the outermost channels does not have a large effect on the absorption.
- The wall temperature of the simulations was set equal to the inlet temperature of the cooling water. Due to a high cooling water mass flow rate, the water outlet temperature is almost equal to its inlet temperature. In [4] it is shown that for all experiments, the difference between the two temperatures is less than 1 K.

2.3.3. Calculation of the Sherwood number from the experimental measurements

The dimensionless Sherwood number Sh is widely regarded as a key metric in dehumidification research and should therefore also be reported in this work. The method for calculating the Sherwood number from experimental measurements followed the approach outlined by the work of Lee et al. [24]. To determine the Sherwood number, which characterizes the mass transfer from the air to the solution flow, the mass transfer coefficient must first be calculated:

$$\beta_{\text{airSol}} = \frac{\dot{m}_{\text{abs}}}{\rho_{\text{a,in}}\, A_{\text{airSol}}\, \left(X_{\text{a,in}} - X_{\text{s,eq,in}}\right)}, \tag{37}$$

where $X_{\text{s,eq,in}}$ is the equivalent humidity ratio of the solution at the inlet and can be calculated from the inlet temperature and concentration of the solution:

$$X_{\text{s,eq,in}} = X_{\text{a}}\left(T_{\text{s,in}}, p_{\text{w,s,in}}\left(T_{\text{s,in}}, \chi_{\text{w,s,in}}\right)\right). \tag{38}$$

The Sherwood number can then be calculated from the mass transfer coefficient:

$$Sh_{\text{airSol}} = \frac{\beta_{\text{airSol}}\, 2\, L_{\text{y}}}{D_{\text{a}}}, \tag{39}$$

where D_{a} denotes the diffusion coefficient of water vapor in air.

3. Results and discussion

In Section 3.1 the settings of the numerical models for the following simulations are described, with Sections 3.1.1 and 3.1.2 for the CFD and reduced model, respectively. In Section 3.2 the results of the numerical models are compared to the experimental measurements for buildings application and in Section 3.3 the results of the CFD model are compared with the results of the reduced model for conditions as experienced in cold stores.

3.1. Settings of the numerical models

For both models, the diffusion coefficient of water vapor in air is fixed to $2.5 \cdot 10^{-5}$ m^2/s and the diffusion coefficient of water in the solution is fixed to $8.34 \cdot 10^{-11}$ m^2/s, equivalent to [4].

All fluid properties are evaluated at the inlet conditions and kept constant during the simulation. For the air flow, the relevant inlet

conditions are the temperature $T_{a,in}$ and relative humidity $\Phi_{a,in}$ and for the solution flow, the relevant inlet conditions are the temperature $T_{s,in}$ and concentration $\chi_{s,in}$. The heat of vaporization is evaluated at the solution inlet temperature. The solution properties are obtained by interpolating data given by *Evonik Industries AG* for the ionic liquid. However, due to a non-disclosure agreement, the data cannot be shown here.

3.1.1. Numerical settings of the CFD model

With the assumptions made in Section 2.1.2, the flows in both mixtures can be solved independently from each other and prior to the heat and mass transfer problem, serving as an input.

To solve the flow in the air, the already available simpleFoam solver from the open source CFD software package OpenFOAM is employed. The flow is solved for a two dimensional x-y plane and is subsequently mapped on the full three dimensional domain. Computation is terminated when the normalized residuals of the solution of the pressure and velocity equations drop below 10^{-6} and 10^{-7}, respectively.

The flow in the solution can be obtained analytically by integrating Eq. (2) with the no-slip and free-slip boundary conditions at the wall and interface, respectively, assuming a developed flow profile, which gives the known Nusselt profile:

$$u_{z,s} = \frac{g}{2\nu_s}\left(\delta_{Nu}^2 - y^2\right), \tag{40a}$$

$$\delta_{Nu} = \left(\frac{3\,\nu_s\,\dot{m}_{s,in}}{\rho_s\,g\,L_x}\right)^{1/3}. \tag{40b}$$

For the evaluation of the heat and mass transfer problem a new solver including implementations for the coupling conditions at the interface was written for the OpenFOAM software. Computation of the heat and mass transfer problem is terminated when the normalized residuals of the solution of both the temperature and water mass concentration equations drop below $5 \cdot 10^{-10}$. Picard iterations are used to deal with the nonlinear boundary condition at the interface for the gradient of the water mass concentration, shown in Eq. (9). The Picard iteration loop is terminated, when the maximum of the residuum vector normalized by the minimum of the current solution vector drops below 10^{-10}.

The mesh in the air region is refined towards the inlet (at $x = 0$) and towards the interface to the solution region (at $y = 0$). In the solution region, the mesh is refined towards the air inlet (at $x = 0$), to obtain a conformal mesh at the interface, and also towards the interface with the air region (at $y = 0$). In Appendix C a mesh study is performed and for each region 160 cells were chosen in the x-direction (direction of air flow), 80 cells in the y-direction (normal direction of interface), and 80 cells in the z-direction (direction of solution flow). This results in 1,024,000 cells per region or 2,048,000 cells in total.

To evaluate the fluid properties of the air, the CoolProp library [25] is used.

3.1.2. Numerical settings of the reduced model

Contrary to the CFD model, the flows are not resolved in the reduced model. For the air flow, correlations for a plane Poiseuille flow with a fixed wall temperature and undeveloped thermal and hydraulic flow profiles at the inlet are used to describe the heat transfer to the solution flow and the Lewis analogy is used to describe the mass transfer.

A grid convergence test, listed in Appendix C, shows that 50 cells are sufficient to describe both the air and solution region, and provide an ample safety margin.

To evaluate the fluid properties of the air, the TIL media library [20] is used.

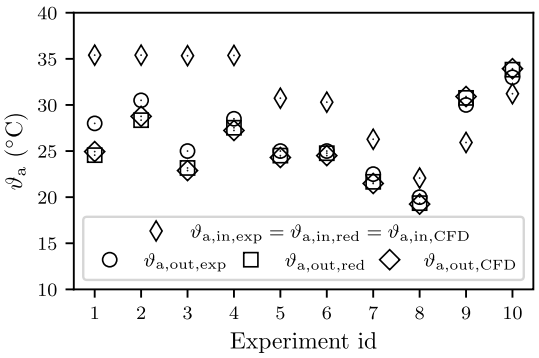

Fig. 6. In- and outlet air temperatures for the selected experiments, and the respective results of the numerical models.

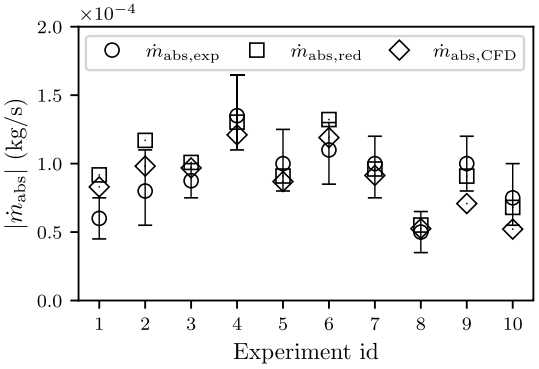

Fig. 7. Magnitude of the absorbed water vapor mass flow rate for the selected experiments, and the respective results of the numerical models. The black bars around the experimental measurements denote the uncertainties.

3.2. Verification of the numerical models with experimental measurements

Ten experiments were performed, replicated by the numerical models and the results compared to the measurements. The parameters of the experiments are listed in Table 1. They were chosen to represent the operating conditions of an air conditioning system in buildings. Temperatures in degrees Celsius are indicated by the symbol ϑ.

Fig. 6 shows the measured air temperatures at the in- and outlet for the experiments (subscript "exp"), as well as the simulated results (subscripts "red" and "CFD" for the reduced and CFD model, respectively). As the inlet conditions, e.g. temperature $\vartheta_{a,in}$, are input parameters to the simulation, there are no differences between $\vartheta_{a,in,exp}$, $\vartheta_{a,in,1D}$ and $\vartheta_{a,in,3D}$. Fig. 7 shows the magnitude of the absorbed water vapor mass flow rate $\dot{m}_{abs}$. Black error bars around the experimental measurements denote the uncertainties. Table 2 presents the experimental measurements for the Sherwood number, air outlet temperature, and absorbed mass flow rate for the ten experiments. It also includes the absolute deviations of the air outlet temperature $\Delta T_{a,out}$ and the relative deviations of the absorbed mass flow rate $\epsilon_{\dot{m}_{abs}}$ for the two numerical models in relation to the experimental measurements, as well as the average and maximum deviations for both models. It is worth noting that the uncertainties of the experiments were not taken into account when calculating the deviations.

Experiments #1 and #2 were done without any cooling of the wall, meaning that the wall may be considered as an adiabatic boundary. However, the solution enters the domain with a lower temperature than the air, so a heat flow rate from the hotter air to the cooler solution exists. For these two experiments the models predict a lower air outlet temperature, suggesting that the models overestimate the heat transfer from the solution to the air. Furthermore, the models estimate a

Table 1
Parameters of the ten experiments for the validation of the models, taken from [4].

id	$u_{a,in}$ (m/s)	$\vartheta_{a,in}$ (°C)	$X_{w,a,in}$ (g_w/kg_{da})	$p_{wv,a,in}$ (Pa)	$\vartheta_{s,in}$ (°C)	$\chi_{d,s,in}$ (% kg_d/kg_s)	$p_{wv,s,in}$ (Pa)	ϑ_{wall} (°C)
#1	0.99	35.40	16.99	2680	15.88	71.80	746	Adiabatic
#2	1.84	35.40	16.73	2655	16.22	72.50	727	Adiabatic
#3	1.02	35.34	16.85	2658	15.97	72.30	725	16.86
#4	1.99	35.37	16.64	2642	16.17	72.30	735	17.99
#5	1.94	30.73	14.44	2293	15.98	67.90	937	17.16
#6	2.01	30.30	13.57	2165	16.93	80.00	397	17.13
#7	1.97	26.28	13.23	2108	17.84	70.93	890	15.53
#8	1.97	22.07	9.81	1549	18.63	70.93	934	15.58
#9	1.97	25.93	9.46	1512	33.70	70.75	2295	36.91
#10	2.00	31.22	11.95	1904	33.88	70.62	2336	37.30

Table 2
Experimental measurements of Sherwood number, air outlet temperature and absorbed mass flow rate for the ten experiments. Additionally, the absolute deviations of the air outlet temperature and the relative deviations of the absorbed mass flow rate of the two numerical models to the experimental measurements are listed. To calculate the deviations between the simulation results and the experimental measurements, the uncertainties of the measurements were not considered.

id	Experiments			CFD model		Reduced model	
	Sh_{airSol} (°C)	$\vartheta_{a,out}$ (°C)	$\dot{m}_{abs}$ (µg/s)	$\Delta T_{a,out,CFD}$ (K)	$\epsilon_{\dot{m}_{abs,CFD}}$ (%)	$\Delta T_{a,out,red}$ (K)	$\epsilon_{\dot{m}_{abs,red}}$ (%)
#1	1.23	28.33	59.46	−3.39	39.58	−3.77	54.34
#2	1.72	30.57	82.19	−1.81	19.44	−2.23	42.34
#3	1.82	25.15	87.87	−2.26	10.25	−1.98	14.79
#4	2.89	28.72	136.22	−1.49	−11.17	−1.19	−4.36
#5	3.00	25.56	102.21	−1.25	−14.95	−1.05	−11.02
#6	2.50	25.35	110.74	−0.84	7.48	−0.58	19.36
#7	3.15	22.31	97.25	−0.82	−6.04	−0.64	−1.21
#8	3.10	19.85	50.18	−0.60	4.69	−0.50	9.86
#9	4.85	30.11	−101.21	0.81	−30.03	0.66	−10.20
#10	6.64	33.49	−77.27	0.44	−32.53	0.34	−11.94
Average deviation	–	–	–	±1.37	±17.62	±1.29	±17.94
Maximum deviation	–	–	–	±3.39	±39.58	±3.77	±54.34

considerably higher absorbed water mass flow rate, so a higher latent heat flow rate is transferred at the interface. Together with the lower air outlet temperature, this indicates that the models underestimate the film surface temperature. This might partly be explained by the vertical grooves in the experiments. As the solution flow thickness is non uniform in the experiments, regions with a higher temperature may exist, where heat cannot be carried away, as no cooler solution exists in its vicinity. Therefore, the solution is unable to take up as much heat, as a solution film with a uniform thickness. Additionally, as previously mentioned in Section 2.2.4, the reduced model approximates the temperature profile in the solution film using a linear approximation. This limitation is particularly restrictive for the adiabatic boundary condition, as it imposes significant constraints on the temperature distribution in the solution film. Experiments #3 and #4 were conducted with approximately the same parameters as experiments #1 and #2, but with a cooled wall. Once again, the models predict a slightly lower air outlet temperature compared to the measurements, but accurately predict the absorbed mass flow rate. In comparison to the adiabatic experiments, the models perform significantly better in predicting the experimental measurements. Only for experiment #3 the absorbed mass flow rate of the reduced model is slightly higher than the measured one, including the uncertainties. This might be explained by the fact that the reduced model does not resolve a concentration profile in the solution film, but assumes a constant solution concentration per cell. Therefore, the constant solution concentration in a single cell is higher at the interface and lower at the wall compared to the experiments and the CFD model, resulting in a lower water vapor pressure at the interface, which increases absorption. Experiments #5 and #6 show the influence of the concentration of the solution at the inlet on the absorption performance, as the solution in experiment #6 has a higher concentration at the inlet, while the other parameters are approximately the same. While the air outlet temperature is not greatly affected, the absorbed mass flow rate increases significantly for experiment #6. This means that the cooled wall is able to deal with the increased cooling load, as the latent heat flow rate is increased. Both models predict the outlet air temperature and the absorbed mass flow rate well, only for experiment #6 the reduced model overestimates the absorbed mass flow rate, including the uncertainties. This might be due to the fact that diffusion in the solution film is not considered in the reduced model and this gets more apparent for higher absorbed mass flow rates. Furthermore, the solution film is significantly thicker for experiment #6, as the solution viscosity is higher, due to the higher concentration. Experiments #7 and #8 represent a two-step absorption process. Both experiments are well replicated by the numerical models and no significant difference between the models can be observed. Experiments #9 and #10 show a two-step desorption, i.e. regeneration, process. While both models replicate the air outlet temperature well, the CFD model suggests significantly lower absorbed mass flow rates than the experiments, while the reduced model predicts the absorbed mass flow rate well. In the experimental setup, the vertical grooves result in a nonuniform thickness of the solution film. In the thinner areas of the solution film, thermal diffusion restricts heat transfer less, while in the thicker areas, due to the round shape of the grooves, there is more surface area for heat exchange with the wall. Therefore, the heat transfer to the wall might be greater in the experiments compared to the models, and therefore the temperature at the film surface might be higher. A higher film surface temperature leads to a higher water vapor pressure, which drives the desorption. However, in the reduced model, heat transfer is described only by conduction, which leads to a higher temperature at the interface, favoring desorption. Nevertheless, it is still not entirely clear why these effects are only evident in the case of desorption at higher solution and air temperatures.

In summary, both models accurately predict the outlet air temperature and are generally within the uncertainties of the measurements for the absorbed water vapor mass flow rate. This is particularly evident in the regular absorption experiments #3 to #8, where both models predict the air outlet temperature with an absolute deviation of less than 2.3 K and the absorbed water vapor mass flow rate with a relative

Table 3
Fixed parameters for comparison of the CFD and reduced model. The parameters represent typical conditions in cold stores.

Description	Equation
Air inlet pressure	$p_{a,in} = 1\,\text{bar}$
Air inlet relative humidity	$\Phi_{a,in} = 80\%$
Solution mass flow rate	$\dot{m}_{s,in} = 1.768 \cdot 10^{-3}\,\text{kg/s}$
Solution inlet temperature	$T_{s,in} = T_{a,in} - 4\,\text{K}$
Solution inlet partial water pressure	$p_{w,s,in} = p_{w,a}(T_{a,in} - 8\,\text{K}, \Phi_{a,in})$
Wall temperature	$T_{wall} = T_{a,in} - 8\,\text{K}$

Table 4
Baseline settings of the parameters for the parameter variation.

Lx	Ly	Lz	$u_{a,in}$	$\vartheta_{a,in}$
100 mm	2 mm	700 mm	2 m/s	6 °C

Table 5
Value ranges of the varied parameters.

Marker shape	Parameter	Values
○	L_x	[25, 50, 75, 100] mm
□	L_y	[1.5, 2, 2.5, 3] mm
▽	L_z	[300, 500, 700, 900] mm
⬡	$u_{a,in}$	[1, 2, 3] m/s
◇	$\vartheta_{a,in}$	[2, 4, 6, 8, 10] °C

deviation of less than 20%, and in many cases, even considerably less. Both models struggle to accurately capture the adiabatic boundary condition on the wall, resulting in generally larger deviations from the experimental measurements compared to the experiments with a cooled wall. The reduced model does not account for mass diffusion within the solution film, which becomes more significant at higher absorbed mass flow rates and thicker solution films. Both models underestimate the desorbed mass flow rate due to the inability to resolve the grooves on the wall of the experiments. However, the reduced model coincidentally performs better in predicting the desorbed mass flow rate, as the approximation of heat transfer in the solution film cancels out the impact of the vertical grooves. For typical cooled absorption processes of falling film absorbers in building applications, the results of both models agree well.

3.3. Comparison of the CFD and reduced model

To compare the results of the CFD and reduced model, selected parameters are varied and the results of both models are compared. The varied parameters are the geometric dimensions L_x, L_y, L_z, the inlet air velocity $u_{a,in}$ and the inlet air temperature $\vartheta_{a,in}$. The results that are being compared are the air outlet temperature $\vartheta_{a,out}$, the absorbed water vapor mass flow rate $\dot{m}_{abs}$ and the air side pressure drop Δp_a. The geometric size of the absorber together with the air outlet temperature and absorbed water vapor mass flow rate can be related to the heat exchange and absorption effectiveness of the absorber. These effectivenesses contribute significantly to the investment costs, as they primarily determine the necessary absorber size. Furthermore, the air side pressure drop of the system determines the required fan power, which ultimately affects the operating costs. Table 3 lists the fixed parameters, for comparison of the two models.

For the parameter variation, one parameter is varied at a time, while the others are kept at baseline settings. Table 4 lists these baseline settings and Table 5 shows the values of the parameters during the parameter variations and the corresponding marker shape for the specific parameter variation in the following figures.

Fig. 8 shows a comparison of the calculated air outlet temperature for the CFD and reduced model. A deviation between the models of

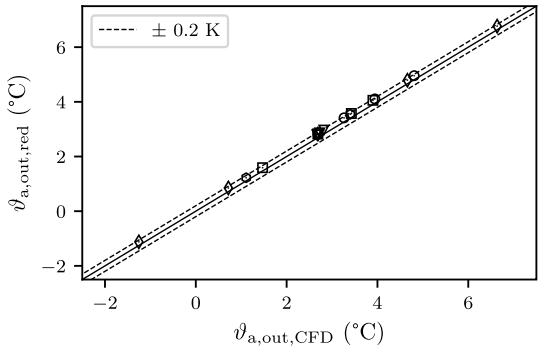

Fig. 8. Comparison of the air outlet temperature obtained by both the CFD and reduced model, for a parameter variation study.

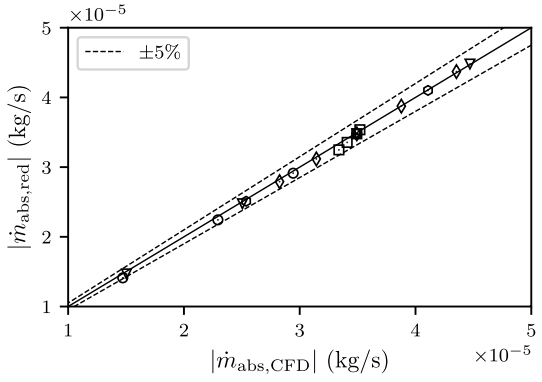

Fig. 9. Comparison of the absorbed water mass flow rate obtained by both the CFD and reduced model, for a parameter variation study.

±0.2 K is marked by dashed black lines. While the reduced model suggests a slightly higher air outlet temperature then the CFD model, the agreement of both models is very good. For all analyzed parameters the agreement is within ±0.2 K and the average deviation is below 0.14 K.

Fig. 9 shows a comparison of the absorbed water vapor mass flow rate between both models. The results of the CFD and reduced model agree well and the relative differences between the models are within ±5% for all parameters. A general over- or underestimation of either model compared to the other cannot be observed and the average deviation for all analyzed parameters is below 1.3%.

Fig. 10 shows the air side pressure drop determined by both models. The results of both models agree well and the relative difference of the pressure drop is below ±5% for almost all analyzed parameters. While the average deviation is below ±3.9%, no general over- or underestimation of one model compared to the other can be identified. Since the heat and mass transfer have no effect on the momentum transfer in the CFD model and the discretization has no effect on the pressure drop calculation in the reduced model, the figure essentially shows a comparison of the pressure drop calculated by the CFD software with the pressure drop given by Stephan [21].

In summary, both models agree very well for the air outlet temperature, the absorbed water vapor mass flow rate, and the air side pressure drop under conditions typical of cold stores.

4. Conclusion

In this work, two numerical models were presented to describe the heat and mass transfer of falling film absorbers with vertical plates: a

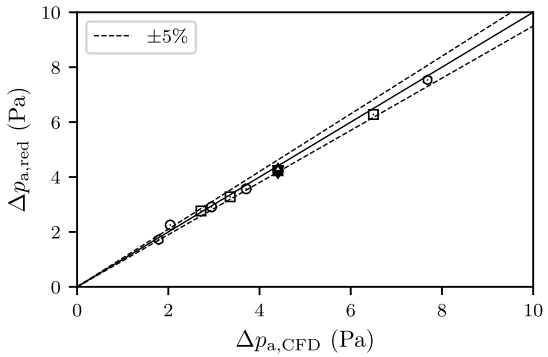

Fig. 10. Comparison of the air side pressure drop obtained by both the CFD and reduced model, for a parameter variation study.

three-dimensional CFD model and a reduced one-dimensional model. The CFD model was created by integrating a heat and mass transfer solver, including user-defined boundary conditions and field functions, into the open-source CFD software package OpenFOAM. This allows the model to be usefully extended, for example to simulate more complex and transient air flows. Based on the CFD model and the knowledge gained about the application, a reduced one-dimensional model was derived by making reasonable assumptions and simplifications.

Both models were compared with experiments conducted in a previous work using an ionic liquid/water working pair for air conditioning in buildings. The models showed good agreement with the measurements, especially in respect to the outlet air temperature. While the reduced model had larger deviations when representing higher absorbed water vapor mass flow rates, the CFD model underestimated the mass flow rate for desorption.

As the models should be used for conditions found in cold stores, the results of both models were compared for typical conditions encountered in these. Great agreement of both models was found for the outlet air temperature, the absorbed water vapor mass flow rate and the air side pressure drop, with average deviations of less then ±0.14 K, ±1.3% and ±3.9%, respectively. While the number of cells used for the CFD model was 2,048,000, the reduced model only used 50 cells. Therefore, the computation time could be reduced from nearly two hours for the CFD model, to approximately 15 s for the reduced model, i.e. by a factor of greater than 400. Moreover, the reduced model can be easily extended for different geometries and serves as a powerful tool for system simulations due to its low computational cost at high accuracy and is well suited for optimization tasks.

Declaration of competing interest

The authors declare the following financial interests/personal relationships which may be considered as potential competing interests: Felix Hochwallner reports financial support was provided by Austrian Research Promotion Agency. Johann Emhofer reports a relationship with Austrian Research Promotion Agency that includes: funding grants.

Data availability

Data will be made available on request.

Acknowledgments

The Austrian Research Promotion Agency (FFG) is gratefully acknowledged for funding this work under Grant No. 874186. Furthermore, the authors thank E. Hofmann and H. Kuhlmann for critical discussion.

Table A.6
Size of the terms of Eq. (20) and the magnitude of their quotient, for the replication of the experiments of Section 3.2.

id	$\dot{Q}_{a,sens}$ (W)	$\dot{Q}_{wv,sens}$ (W)	$\left\lvert\frac{\dot{Q}_{wv,sens}}{\dot{Q}_{a,sens}}\right\rvert$ (%)
1	137.05	0.77	0.57
2	165.63	1.50	0.91
3	158.50	1.03	0.65
4	199.17	2.08	1.05
5	156.33	1.15	0.73
6	144.17	1.55	1.08
7	119.43	0.94	0.79
8	71.25	0.32	0.45
9	−125.15	0.90	0.72
10	−67.42	0.36	0.53

Appendix A. Neglecting a part of the sensible heat flow rate from the air to the solution in the reduced model

In Section 2.2.3, in Eq. (20), a term in the equation of the sensible heat flow rate from the air to the solution was neglected in the reduced model. Revisiting the equation gives:

$$\overbrace{\dot{m}_{da}\left(c_{p,da}+X_{a,in}c_{p,wv}\right)}^{\dot{m}_{a,in}c_{p,a,in}}\left(T_{a,in}-T_{a,out}\right)+ \dot{m}_{abs}c_{p,wv}\left(T_{a,out}-T_{fs}\right)=\dot{Q}_{airSol}. \quad \text{(20 revisited)}$$

The first term $\dot{Q}_{a,sens}=\dot{m}_{a,in}c_{p,a,in}\left(T_{a,in}-T_{a,out}\right)$ describes the necessary sensible heat flow rate to change temperature of the air, that would be present, if no water vapor would be absorbed of it. The second term $\dot{Q}_{wv,sens}=\dot{m}_{abs}c_{p,wv}\left(T_{a,out}-T_{fs}\right)$ needs to be added to the first term, to account for the fact that the absorbed water vapor is cooled or heated to the film surface temperature and not to the air outlet temperature, as the remaining air flow. In Table A.6 both terms and the magnitude of their quotient $\left\lvert\frac{\dot{Q}_{wv,sens}}{\dot{Q}_{a,sens}}\right\rvert$ are listed, for the replication of the experiments of Section 3.2. The magnitude of the first term $\dot{Q}_{a,sens}$ ranges from 67.24 to 199.17 W, while the magnitude of the second term $\dot{Q}_{wv,sens}$ ranges from 0.32 to 2.08 W. Therefore, the magnitude of the second term, that is being neglected in the reduced model, is only between 0.45 and 1.08% of the magnitude of the first term.

Appendix B. Simplification in the Lewis analogy

In [22] the Lewis analogy is derived, which gives a relationship between the heat and mass transfer coefficients, the mass transfer coefficient is related to the difference in mass fraction, i.e. the specific humidity of moist air, between the two phases. To separate the heat transfer from the mass transfer in the reduced model, the mass transfer coefficient, as obtained by the Lewis analogy, is used as if it was related to the difference in humidity ratio. To estimate the error made by this simplification, we compare the specific humidity to the humidity ratio.

The humidity ratio X_a can be derived from the water mass fraction $\chi_{w,a}$ as stated in Eq. (12):

$$X_a=\frac{\chi_{w,a}}{1-\chi_{w,a}}. \quad \text{(12 revisited)}$$

Both the water mass fraction, as well as the humidity ratio are typically in the order of 10^{-3} for moist air. Therefore, the difference between both quantities is small, mostly well below 1%. Furthermore, for low air temperatures the absolute values of the water mass fraction and humidity ratios cannot exceed high values before saturation is reached and as the models shall be used for simulations at conditions as experienced in cold stores, low air temperatures are expected. Since the difference between the specific humidity and the humidity ratio is very small, the error of this simplification is small. However, this simplification allows the derivation of equations for the absorbed water vapor mass flow rate (18) and the transferred sensible heat flow rate (25) that can be solved analytically and independently from each other.

Table C.7
Simulation parameters for the mesh study.

Parameter	Value
Lx	100 mm
Ly	2 mm
Lz	700 mm
$u_{a,in}$	2 m/s
$\vartheta_{a,in}$	6 °C
$\Phi_{a,in}$	80%
$\dot{m}_{s,in}$	$1.768 \cdot 10^{-3}$ kg/s
$\vartheta_{s,in}$	2 °C
$\chi_{d,s,in}$	69.7%
ϑ_{wall}	−2 °C

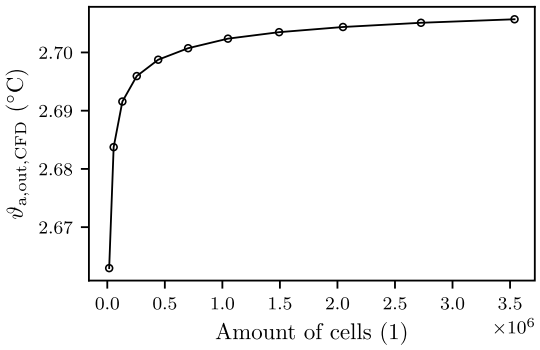

Fig. C.11. Air outlet temperature in dependence on the amount of cells for the CFD model.

Appendix C. Mesh study and required computation time

To verify the convergence of the meshes, simulations of both models were performed with fixed simulation parameters but an increasing number of cells and the outlet air temperature and humidity ratio were documented. In Table C.7 the simulation parameters are listed. In addition, the calculation times of the simulations are given.

For validity checking of the CFD model, the calculated velocity, temperature and water concentration profiles were compared to results by Emhofer et al. [4] and a good agreement was found. Figs. C.11 and C.12 show the calculated outlet air temperature and humidity ratio depending on the number of cells, respectively. Although slight changes are observed in both quantities as the number of cells increases, a total of 2,048,000 cells (160 × 160 × 80 grid) were chosen equally distributed over both region, to achieve high accuracy at a reasonable computational cost. The relative difference for the outlet air temperature and humidity ratio between 2,048,000 and 3,538,944 cells is less than 0.02% and 0.06%, respectively.

C.1. CFD model

The simulations of the CFD model were done on a GNU/Linux CentOS 7 machine on an AMD EPYC 7302 CPU, parallelized into four processes, and one simulation took approximately 1 h and 50 min with 2,048,000 cells used.

C.2. Reduced model

Figs. C.13 and C.14 show the air outlet temperature and humidity ratio depending on the number of cells, respectively. Although the relative difference between 20 and 50 cells is below 0.01% for both the air outlet temperature and humidity ratio, 50 cells were used for the simulations in this work, providing a fair margin of safety.

The simulations of the reduced model were done on a Windows 10 machine with an Intel Xeon W-2235 CPU and one simulation took approximately 15 s with 50 cells used.

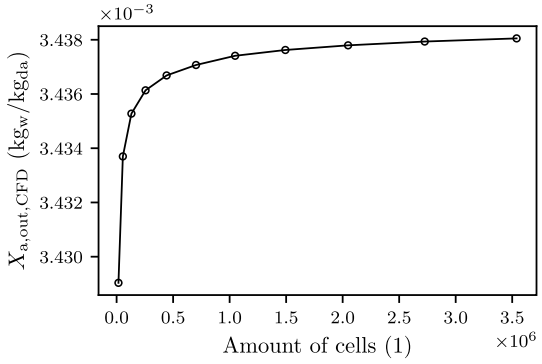

Fig. C.12. Air outlet humidity ratio in dependence on the amount of cells for the CFD model.

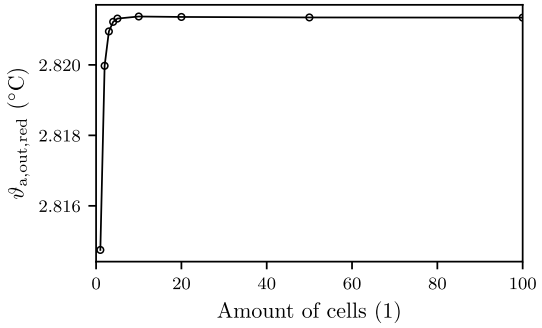

Fig. C.13. Air outlet temperature in dependence on the amount of cells for the reduced model.

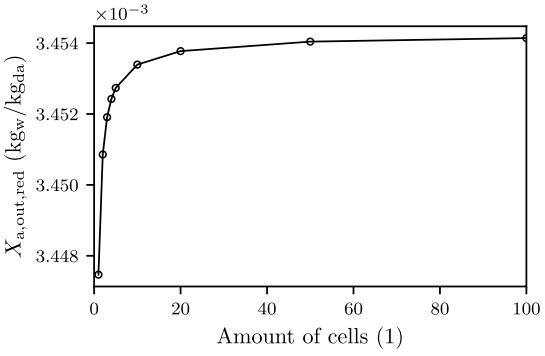

Fig. C.14. Air outlet humidity ratio in dependence on the amount of cells for the reduced model.

References

[1] IEA, The Future of Cooling, place: paris, 2018, URL https://www.iea.org/reports/the-future-of-cooling.

[2] Z. Li, X.-H. Liu, Z. Lun, Y. Jiang, Analysis on the ideal energy efficiency of dehumidification process from buildings, Energy Build. 42 (11) (2010) 2014–2020, http://dx.doi.org/10.1016/j.enbuild.2010.06.008.

[3] S.S. Elsayed, T. Miyazaki, Y. Hamamoto, A. Akisawa, T. Kashiwagi, Performance analysis of air cycle refrigerator integrated desiccant system for cooling and dehumidifying warehouse, Int. J. Refrig. 31 (2) (2008) 189–196, http://dx.doi.org/10.1016/j.ijrefrig.2007.07.002.

[4] J. Emhofer, B. Beladi, P. Dudzinski, T. Fleckl, H.C. Kuhlmann, Analysis of a cross-flow liquid-desiccant falling-film, Appl. Therm. Eng. 124 (2017) 91–102, http://dx.doi.org/10.1016/j.applthermaleng.2017.05.130.

[5] J.D. Killion, S. Garimella, A critical review of models of coupled heat and mass transfer in falling-film absorption, Int. J. Refrig. 24 (8) (2001) 755–797, http://dx.doi.org/10.1016/S0140-7007(00)00086-4.
[6] V.E. Nakoryakov, N.I. Grigor'eva, Combined heat and mass transfer during absorption in drops and films, J. Eng. Phys. 32 (3) (1977) 243–247, http://dx.doi.org/10.1007/BF00865776.
[7] G. Grossman, Simultaneous heat and mass transfer in film absorption under laminar flow, Int. J. Heat Mass Transfer 26 (3) (1983) 357–371, http://dx.doi.org/10.1016/0017-9310(83)90040-6.
[8] M.S. Park, J.R. Howell, G.C. Vliet, J. Peterson, Numerical and experimental results for coupled heat and mass transfer between a desiccant film and air in cross-flow, Int. J. Heat Mass Transfer 37 (1994) 395–402, http://dx.doi.org/10.1016/0017-9310(94)90039-6.
[9] S. Karami, B. Farhanieh, A numerical study on the absorption of water vapor into a film of aqueous LiBr falling along a vertical plate, Heat Mass Transf. 46 (2) (2009) 197–207, http://dx.doi.org/10.1007/s00231-009-0557-y.
[10] E. Hofmann, H.C. Kuhlmann, On the optimum mass transfer of flat absorbing falling films, Int. J. Heat Mass Transfer 55 (25–26) (2012) 7686–7697, http://dx.doi.org/10.1016/j.ijheatmasstransfer.2012.07.074.
[11] R. Qi, C. Dong, L.-Z. Zhang, Development of liquid-air mass transfer correlations for liquid desiccant dehumidification considering the liquid/air contact and film instability, Int. J. Heat Mass Transfer 141 (2019) 491–502, http://dx.doi.org/10.1016/j.ijheatmasstransfer.2019.06.099, URL https://linkinghub.elsevier.com/retrieve/pii/S001793101932215X.
[12] T. Wen, L. Lu, Y. Luo, Review on the fundamentals and investigations of falling film dehumidification/absorption refrigeration based on CFD technology, Int. J. Heat Mass Transfer 171 (2021) 121042, http://dx.doi.org/10.1016/j.ijheatmasstransfer.2021.121042.
[13] Y. Luo, H. Yang, L. Lu, Liquid desiccant dehumidifier: Development of a new performance predication model based on CFD, Int. J. Heat Mass Transfer 69 (2014) 408–416, http://dx.doi.org/10.1016/j.ijheatmasstransfer.2013.10.033.
[14] Y. Luo, Y. Chen, H. Yang, Y. Wang, Study on an internally-cooled liquid desiccant dehumidifier with CFD model, Appl. Energy 194 (2017) 399–409, http://dx.doi.org/10.1016/j.apenergy.2016.05.133.
[15] H.G. Weller, G. Tabor, H. Jasak, C. Fureby, A tensorial approach to computational continuum mechanics using object-oriented techniques, Comput. Phys. 12 (6) (1998) 620, http://dx.doi.org/10.1063/1.168744.
[16] C. Truesdell, R. Toupin, The Classical Field Theories, in: S. Flügge (Ed.), Principles of Classical Mechanics and Field Theory / Prinzipien Der Klassischen Mechanik Und Feldtheorie, in: Encyclopedia of Physics / Handbuch der Physik, vol. 2 / 3 / 1, Springer Berlin Heidelberg, Berlin, Heidelberg, 1960, pp. 226–858, http://dx.doi.org/10.1007/978-3-642-45943-6.
[17] S. Bo, X. Ma, Z. Lan, J. Chen, H. Chen, Numerical simulation on the falling film absorption process in a counter-flow absorber, Chem. Eng. J. 156 (3) (2010) 607–612, http://dx.doi.org/10.1016/j.cej.2009.04.066, URL https://linkinghub.elsevier.com/retrieve/pii/S1385894709003222.
[18] P. Fritzson, P. Bunus, Modelica - a general object-oriented language for continuous and discrete-event system modeling and simulation, in: Proceedings 35th Annual Simulation Symposium. SS 2002, IEEE Comput. Soc, San Deigo, CA, USA, 2002, pp. 365–380, http://dx.doi.org/10.1109/SIMSYM.2002.1000174, URL http://ieeexplore.ieee.org/document/1000174/.
[19] M. Dempsey, Dymola for Multi-Engineering Modelling and Simulation, in: 2006 IEEE Vehicle Power and Propulsion Conference, IEEE, Windsor, UK, 2006, pp. 1–6, http://dx.doi.org/10.1109/VPPC.2006.364294, URL http://ieeexplore.ieee.org/document/4211322/.
[20] TLK-Thermo GmbH, TIL Suite - Simulates thermal systems, place: braunschweig, 2022, URL https://tlk-thermo.com/index.php/en/software/til-suite.
[21] K. Stephan, Wärmeübergang und Druckabfall bei nicht ausgebildeter Laminarströmung in Rohren und in ebenen Spalten, Chem. Ing. Tech. 31 (12) (1959) 773–778, http://dx.doi.org/10.1002/cite.330311204, Publisher: John Wiley & Sons, Ltd.
[22] H.D. Baehr, K. Stephan, Wärme- Und Stoffübertragung, Springer Berlin Heidelberg, Berlin, Heidelberg, 2019, http://dx.doi.org/10.1007/978-3-662-58441-5.
[23] J. Emhofer, T. Fleckl, Visualization of the microscopic flow profile of state-of-the-art absorption heat pump working pairs under operational conditions, Appl. Therm. Eng. 73 (1) (2014) 66–73, http://dx.doi.org/10.1016/j.applthermaleng.2014.07.026.
[24] J.H. Lee, C.W. Jung, Y.S. Chang, J.T. Chung, Y.T. Kang, Nu and Sh correlations for LiCl solution and moist air in plate type dehumidifier, Int. J. Heat Mass Transfer 100 (2016) 433–444, http://dx.doi.org/10.1016/j.ijheatmasstransfer.2016.04.100, URL https://linkinghub.elsevier.com/retrieve/pii/S0017931016301946.
[25] I.H. Bell, J. Wronski, S. Quoilin, V. Lemort, Pure and Pseudo-pure Fluid Thermophysical Property Evaluation and the Open-Source Thermophysical Property Library CoolProp, Ind. Eng. Chem. Res. 53 (6) (2014) 2498–2508, http://dx.doi.org/10.1021/ie4033999, Publisher: American Chemical Society.